Knot-inspired optical sensors for slip detection and friction measurement in dexterous robotic manipulation

Jing Pan, Qi Wang, Shuaikang Gao, Zhang Zhang, Yu Xie, Longteng Yu and Lei Zhang

---

Related articles

All-fiber ellipsometer for nanoscale dielectric coatings
Jose Javier Imas, Ignacio R. Matías, Ignacio Del Villar, Aritz Ozcáriz, Carlos Ruiz Zamarreño, Jacques Albert
Opto-Electronic Advances   2023 **6**, 230048   doi: 10.29026/oea.2023.230048

Specialty optical fibers for advanced sensing applications
Huanhuan Liu, Dora Juan Juan Hu, Qizhen Sun, Lei Wei, Kaiwei Li, Changrui Liao, Bozhe Li, Cong Zhao, Xinyong Dong, Yuhan Tang, Yihong Xiao, Gerd Keiser, Perry Ping Shum
Opto-Electronic Science   2023 **2**, 220025   doi: 10.29026/oes.2023.220025

Multifunctional flexible optical waveguide sensor: on the bioinspiration for ultrasensitive sensors development
Arnaldo Leal-Junior, Leticia Avellar, Vitorino Biazi, M. Simone Soares, Anselmo Frizera, Carlos Marques
Opto-Electronic Advances   2022 **5**, 210098   doi: 10.29026/oea.2022.210098

More related article in Opto-Electron Journals Group website

Knot-inspired optical sensors for slip detection and friction measurement in dexterous robotic manipulation

Jing Pan[1], Qi Wang[1], Shuaikang Gao[1], Zhang Zhang[1], Yu Xie[1], Longteng Yu[1]* and Lei Zhang[1,2]*

Friction plays a critical role in dexterous robotic manipulation. However, realizing friction sensing remains a challenge due to the difficulty in designing sensing structures to decouple multi-axial forces. Inspired by the topological mechanics of knots, we construct optical fiber knot (OFN) sensors for slip detection and friction measurement. By introducing localized self-contacts along the fiber, the knot structure enables anisotropic responses to normal and frictional forces. By employing OFNs and a change point detection algorithm, we demonstrate adaptive robotic grasping of slipping cups. We further develop a robotic finger that can measure tri-axial forces via a centrosymmetric architecture composed of five OFNs. Such a tactile finger allows a robotic hand to manipulate human tools dexterously. This work could provide a straightforward and cost-effective strategy for promoting adaptive grasping, dexterous manipulation, and human-robot interaction with tactile sensing.

Keywords: robotic perception; adaptive grasping; slip detection; force decoupling; polymer optical fiber

Introduction

Human hands can precisely perceive friction through mechanical receptors in the skin, which enables us to perform sophisticated tasks such as adaptive grasping, folding, twisting, etc.[1] Similarly, artificial tactile perception, especially friction measurement and slip detection, plays a vital role in dexterous robotic manipulation[2–4]. Over the last decade, soft and flexible tactile sensors based on electrical[5–12], magnetic[13–15], and optical[16–20] principles have been developed for robotic applications[21–23]. Among them, sensors based on optical waveguides[24–29] have attracted particular interest due to their excellent

flexibility[30,31], high sensitivity[32], multi-modality[33,34], and distributed sensing capability[35,36], as well as anti-electromagnetic interference and corrosion-resistance characteristics[37]. Several attempts have been made to improve robotic manipulation using optical waveguides. For example, Leal et al. report a bioinspired multifunctional flexible optical sensor (BioMFOS) as an ultrasensitive tool for force (intensity and location) and orientation sensing[27]. Li et al. embedded a silica microfiber probe-based optical neuron into thin PDMS to detect and recognize the motions of a robotic finger[38].

To provide informative state feedback during grasping,

Teeple et al. incorporated optical waveguides in a soft gripper for proprioception and contact force sensing for deep-sea grasping[31]. This approach, however, was limited to normal force measurement since lossy optical waveguides with axisymmetric cross-sections are generally insensitive to tangential perturbations. To overcome this limitation, we attached fingerprint-like ridges to an optical microfiber sensor in our previous work[39]. The ridges enhanced friction-induced vibration, which was perceived by the optical fiber underneath. Although slip was successfully detected with high sensitivity, the decoupling between normal and frictional forces remained to be resolved.

In fact, the prerequisite for friction measurement lies in the anisotropic structure or material of a sensor. Recently, Zhou et al. encapsulated a pair of soft optical waveguides in an elastomeric slab with a crossed-over layout[40]. Each waveguide exhibited anisotropic responses to tri-axial forces. Through a decoupling algorithm based on multiple linear fitting, the optical sensor could measure normal and frictional forces, respectively. Nevertheless, the 3 mm-thick optical skin was inconvenient to incorporate into the robotic hand. As such, it is desirable to construct highly integrated robotic tactile sensors based on optical waveguides for friction measurement.

Inspired by the topological mechanics of knots[41], we propose a cost-effective strategy for friction sensing based on optical fiber knots (OFN) in this work. The knot structure alters the load distribution along the fiber, making a single polymer fiber sensitive to both normal and frictional forces. The OFN sensor achieved a maximum sensitivity of 2.67 N^{-1} for normal force detection and 5.59 N^{-1} for frictional force detection, respectively. By fixing OFN sensors onto the finger pads, we demonstrated that a robotic gripper could adaptively grasp a cup based on slip feedback using a change point detection algorithm[42]. We further devised a robotic tactile finger that can measure tri-axial forces via a self-decoupling approach. Five OFN sensors were arranged in a centrosymmetric layout inside the finger to measure forces from various directions independently. Equipped with the tactile finger, a robotic gripper achieved dexterous manipulation of human tools such as a knife and a key.

Our OFN-based sensing strategy could be a straightforward and cost-effective solution for tactile perception-assisted dexterous robotic manipulation. By incorporating these sensors, we have achieved high sensitivity, flexibility, and scalability, enabling robots to interact more efficiently with their environment. This technology has diverse applications in industrial automation, prosthetics, and healthcare robotics.

Results and discussion

An optical fiber knot with force sensing capability

Knots demonstrate intriguing mechanical properties arising from their topological structure[41]. The entangled architecture facilitates interaction between different sections along a fiber, which is beneficial to enhancing the sensitivity of fiber sensors[43], fabricating smart fabrics[44], and assembling optical resonators[45]. Inspired by the topological mechanics of knots, we fabricated a compact tactile sensor by encapsulating an OFN in polydimethylsiloxane (PDMS) (Fig. 1(a)). Polymer optical fiber (PMMA) has been selected for fabricating the fiber knot due to its relatively high mechanical strength (Young's modulus of 3 to 4 GPa) and the ease of knotting operation. While microfiber could also be utilized in constructing knot structures, their intricate knotting process and limited dynamic range make them challenging to meet the demands for robotic tactile sensing applications. The PDMS encapsulation not only maintains the knot structure but also enhances the mechanical damage threshold of the sensor (Fig. S1). However, the OFN sensor faces limitations in terms of heat insulation capability due to the properties of PDMS and the thermal stability of PMMA. As a result, this combination may not be able to withstand high ambient temperatures effectively. It is suggested to maintain the temperature below 60 °C (Fig. S2). A light emitting diode (LED) and a photodetector (PD) were coupled with the fiber ends to operate as the light source and the receiver, respectively (Fig. S3). To ensure consistency in size, we fastened the PMMA fiber knot around a polymer cylinder mold (see Figs. S4 and S5). A sensing array with multiple identical OFNs can be readily fabricated using the mold (Fig. 1(b)). The pressure response of each individual OFN in the array is illustrated in Fig. S6, which exhibits decent consistency across the OFNs, ensuring reliable and consistent pressure sensing performance.

To explore the effect of force, we poked the sensor with a plastic rod and observed the light intensity from the output end (Fig. 1(c–e)). The fundamental operating mechanism of the OFN sensor is based on the micro-
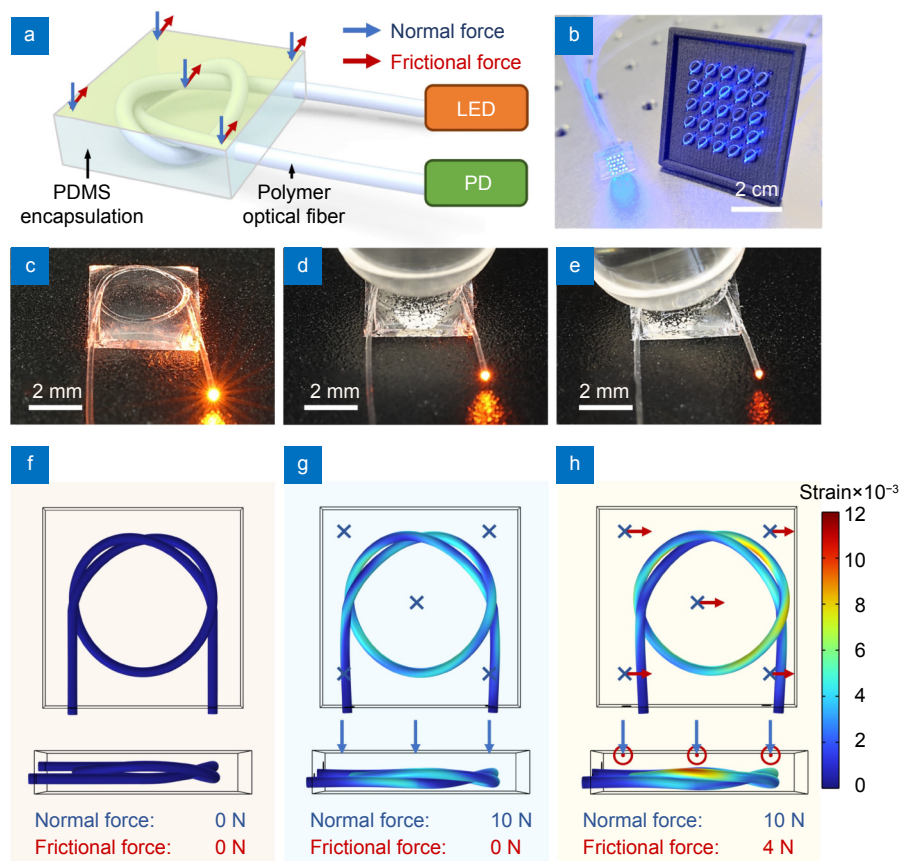
Fig. 1 | Overview of the OFN sensor. (a) Schematic diagram of the OFN sensing system. (**b**) 5 by 5 OFN sensing array. (**c**) Photographs of the output light when the sensor was untouched, (**d**) subjected to normal force, and (**e**) subjected to both normal and frictional force. (**f**) Finite element simulations of strain distribution when the OFN sensor (knot diameter: 3.5 mm, side length: 5 mm, thickness: 1 mm) was untouched, (**g**) subjected to a 10 N normal force, and (**h**) subjected to a 10 N normal force and an additional 4 N frictional force, respectively.

bending loss[46] at the points where the fiber overlaps with itself. When a normal force or a frictional force is applied to the knot, the fiber squeezes against itself at the points of overlap, intensifying the bending loss, thereby decreasing the output intensity of the sensor. This effect is illustrated by the ray diagrams shown in Fig. S7. To understand the working mechanism, we carried out finite element simulations, where an OFN embedded PDMS slab was subjected to normal and frictional forces (Fig. 1(f–h)). Both forces were evenly distributed over the top surface of the slab. For clarity, the slab is hidden in the figures and only the undeformed state is outlined. When the normal force was applied, the knot became more compressed with strain concentrated near the crossings (Fig. 1(g)). As the frictional force was then superimposed, the knot deformed sideways and the strain increased significantly, especially within the segment being pushed away (Fig. 1(h)). These elastic deformations induced localized micro-bends at the crossings, which caused the transmitted mode to exceed the critical angle.

Consequently, the transmitted light was refracted into the cladding and lost from the fiber. In other words, the knotted structure introduced self-contacts at multiple locations along the fiber, making the fiber sensitive to forces from various directions. Being sensitive to both normal and frictional forces, the OFN can be a promising candidate for slip detection and tri-axial force measurement in robotic manipulation.

Characterization of normal and frictional forces measurement

Next, we investigated the sensing characteristics of the OFN sensor for measuring normal and frictional forces. OFNs with different knot diameters (4.5 mm, 3.5 mm, and 2.5 mm) were separately embedded in square PDMS slabs (side lengths of 5 mm and thicknesses of 1 mm). Here, the knot diameter is defined as the diameter of the inscribed circle of the knot. For clarity, we refer to these slab-encapsulated OFNs as "flat OFN sensors". Figure 2(a) illustrates the force testing platform in which the

testing probe is driven by a tri-axial motorized stage, and the applied force is recorded via a multi-axis force sensor. As Fig. 2(b) shows, a sensor with a smaller knot diameter responded more drastically to the normal force, since a smaller knot may cause severer micro-bending. Specifically, the sensitivity of the 2.5 mm knot to normal force was calculated to be 2.67 N^{-1}, which is much higher than that of the 4.5 mm knot with a sensitivity of 0.45 N^{-1}.

We then tested the response of a 2.5 mm knot to static frictional forces. The maximum frictional force that can be applied on the sensor is proportional to the normal force between the testing probe and the sensor. The sensitivity to frictional force was relatively unaffected by the pre-loaded normal force (Fig. 2(c)), which was 2.07 N^{-1}, 4.24 N^{-1}, 6.36 N^{-1}, and 5.59 N^{-1} under pre-loaded normal forces of 2.5 N, 5 N, 7.5 N, and 10 N, respectively. In addition, the sensing range broadened from 0–1 N to 0–4 N when the normal force increased from 2.5 N to 10 N. These results are in consistent with the Coulomb friction model (the maximum friction is linearly proportional to the normal force) and denote a coefficient of friction of 0.4 between the sensor and the probe.

The responsiveness of the flat OFN sensor was examined afterward. A step force in either the normal or tangential direction was exerted on the sensor before a sudden release (Fig. 2(d)). Both response time and recovery time were measured to be 50 ms, which was prob-ably limited by the elastomeric encapsulation. Nevertheless, this encapsulation protected the OFN and thereby boosted the robustness of the sensor. To prove this, we applied a 5 N normal force and a 1 N frictional force (pre-loaded normal force: 0.4 N) on the sensor for more than 1500 times (Fig. 2(e) and Fig. 2(f)). The smooth envelopes of the time series data verified the good stability and robustness of the sensor.

Adaptive grasping based on slip detection

The friction sensing capability of the flat OFN sensor is conducive to adaptive robotic grasping. First, we constructed a slip detection system comprising two flat OFN sensors and a slip detection program named Slip Finder. Based on a change point detection algorithm[36], the program detects slip-induced perturbations in the signal by giving a Slip Score (1: a slip occurs, 0: no slips) in real time.

As shown in Fig. 3(a), we commanded a two-fingered robotic gripper to grasp a plastic cup that would slip downward if weights were added into it. Two flat OFN sensors were fixed to one finger pad of the gripper (Fig. S8), such that both translational slip and rotational slip could be detected. By dropping screws into the cup, we created a slipping tendency for the cup, increasing the frictional force on the sensors. Figure 3(b) presents the sensing signals of the whole process. Initially, the signal
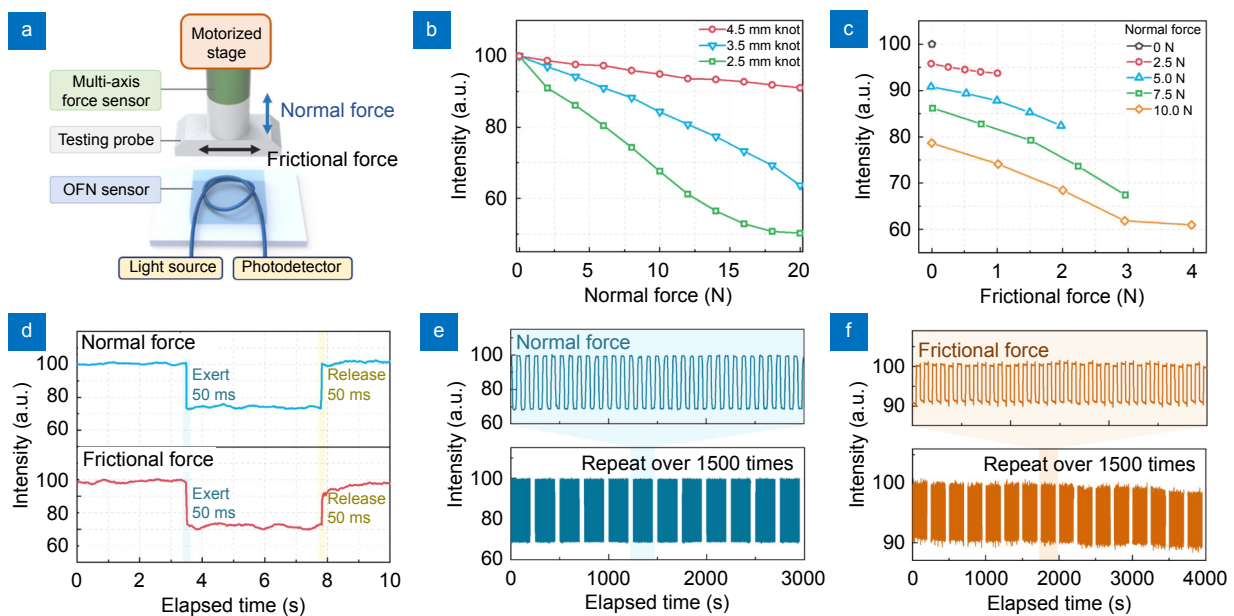

Fig. 2 | Characterization of normal and frictional force sensing. (**a**) Schematic diagram of the friction testing system. (**b**) Responses to normal force of OFN sensors with knot diameters of 4.5 mm, 3.5 mm and 2.5 mm. (**c**) Responses to frictional force of OFN sensors with a diameter of 2.5 mm when pre-loaded with 0 N, 2.5 N, 5 N, 7.5 N and 10 N normal forces. (**d**) Intensity signals of the OFN sensor loaded/unloaded with normal and frictional forces. (**e, f**) Intensity signals during cyclical loading of normal force and frictional force, respectively.
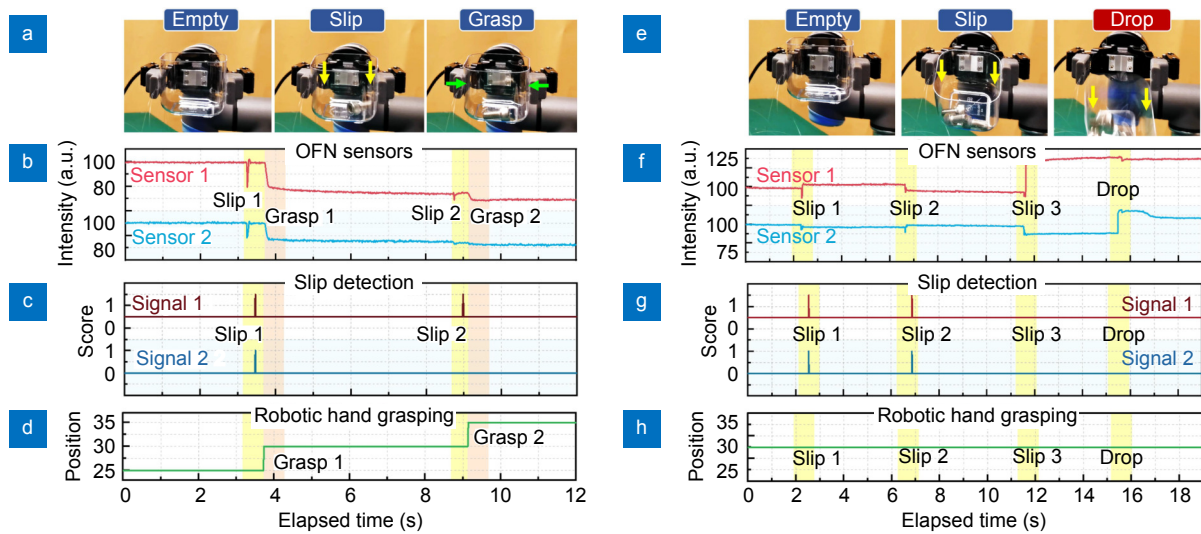
Fig. 3 | Adaptive grasping based on slip detection when the slip feedback is ON and OFF, respectively. (**a**, **e**) Snapshots during the experiments. Yellow arrows indicate slips of the cup while green arrows indicate closing of the robotic hand. (**b**, **f**) Real-time signals of the OFN sensors. (**c**, **g**) Real-time scores calculated by the Slip Finder program. Slip Score = 1: a slip occurred, Slip Score = 0: no slips. (**d**, **h**) Real-time position of the robotic fingers. Position = 0: fully open, Position = 255: fully closed.

remained stable when the cup was grasped firmly. When a screw was dropped into the cup, the grip strength of the robotic gripper was insufficient to hold the cup, resulting in a downward slip (see Supplementary Movie S2). Instantly, both OFN sensors captured the perturbation caused by the slip, which appeared as spikes in the real-time signal (yellow columns in Fig. 3(b)). Slip Finder promptly generated a Slip Score of "1" (Fig. 3(c)), and subsequently, the robotic gripper closed further to suppress slipping (Fig. 3(d)). Here, the closing degree is represented by the Finger Position, a built-in parameter of the robotic gripper, with 0 indicating fully open and 255 indicating fully closed. As the robotic gripper closed more, the pressure on the fingers increased, and the light intensities decreased (red columns in Fig. 3(b)). Since the grip strength had been intensified, the cup only tilted slightly when the second screw was released at approximately 8.5 s, leading to a local rotational slip. Consequently, only one sensor responded (Fig. 3(c)), yet the robotic gripper still reacted swiftly (Fig. 3(d)). Although three more screws were dropped into the cup later, the cup did not slip out from the gripper.

In contrast, when we cut the feedback from Slip Finder, the robotic gripper failed to prevent the cup from dropping (Fig. 3(e) and Movie S3). As Fig. 3(f, g) shows, when the first two screws dropped into the cup, two slips were accurately identified. However, the robotic gripper took no action (Fig. 3(h)) due to the lack of closed-loop grasping control. After the third screw was released, the

cup slanted and detached from the sensors, resulting in an invalid slip detection. Finally, the fourth screw caused the cup to drop. These two experiments suggest that our slip detection system can effectively assist adaptive robotic grasping.

Characterization of tri-axial force sensing

It is clear that the OFN holds promise in tri-axial force sensing, but the normal and frictional forces were coupled together in our initial study presented above. To tackle this problem, we fabricated a 'cubic OFN sensor' by placing an OFN at the midplane of a PDMS cube. As such, orthogonal forces (denoted as F_x, F_y, and F_z) could be separately applied on the front, side, and top surfaces of the cubic OFN sensor (Fig. 4).

To investigate the characteristics of tri-axial force sensing, we compressed the cubic OFN sensor on different surfaces by adjusting its orientation (Fig. 4(a)). Three sizes of cubic OFN sensors were tested, with knot diameters of 4.5 mm, 3.5 mm, and 2.5 mm and side lengths of 5 mm, 4 mm, and 3 mm, respectively. As shown in Fig. 4(b–d), all three sensors were sensitive to F_y and F_z, whereas their responses to F_x were weak. Since the knot was covered with a thick layer of PDMS in the F_x direction, its deformation due to F_x was much slighter than that caused by F_y and F_z. Additionally, similar to the flat OFN sensors, cubic OFN sensors with smaller knot diameters demonstrated higher sensitivities in both F_y and F_z. For example, the sensitivity of the 2.5 mm knot
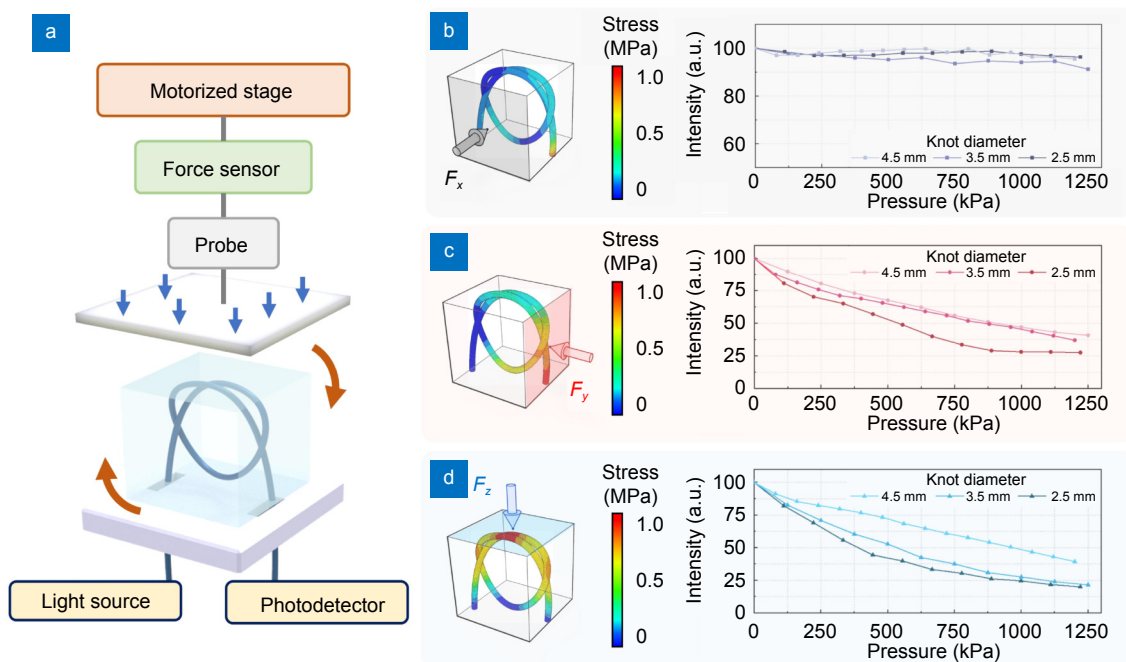
Fig. 4 | Characterization of tri-axial force sensing. (**a**) Schematic diagram of the tri-axial force testing system. (**b–d**) Stress distribution and responses of OFN sensors with knot diameters of 4.5 mm, 3.5 mm, and 2.5 mm to F_x, F_y, and F_z, respectively.

reached 125.21 MPa^{-1} in the F_z direction, which is remarkably higher than the 50.52 MPa^{-1} sensitivity of the 4.5 mm knot. Although the sensitivity can be improved by reducing the knot diameter, the detection range will inevitably become narrower as there is a bending limit for the fiber. Moreover, forcefully tightening the knot could potentially cause plastic deformation of the fiber, thereby compromising the consistency and sensitivity of the sensor (Fig. S9). Considering the trade-off between sensitivity and detection range, the 3.5 mm knot was selected for the following experiments.

Dexterous manipulation based on tri-axial force sensing

The tri-axial forces at the fingertips provide the robot with rich information about the motion state of the grasped object. By monitoring tri-axial forces, the robot can sense critical moments during manipulation and react accordingly. To this end, we devised a robotic tactile finger that can measure tri-axial forces with a group of cubic OFN sensors (Fig. 5(a)). As illustrated in Fig. 5(b, c), five cubic OFN sensors are arranged in a centrosymmetric layout, such that sensors No. 1 to No. 5 measure $-F_x$, $-F_y$, $+F_x$, $+F_y$, and F_z, respectively. The tails of all knots extend downwards to facilitate wire collection and sensor installation. When the black contact plate is subjected to an external force, the compressive force is first

applied to sensor No. 5 in the blue slider through the square column. The frictional force then drives the blue slider to move sideways and compress sensors No. 1 to No. 4 through the yellow cylinders. In line with the characteristics shown in Fig. 4, sensors No. 1 to No. 4 are compressed from their local y directions, and sensor No. 5 is compressed from its local z direction. In this way, the external force is mechanically decomposed into separate components, which can be measured independently by the five sensors, realizing a self-decoupling approach to tri-axial force sensing.

We fabricated a pair of the tactile fingers (Fig. 5(d)) and integrated them into a robotic gripper. Experiments imitating human operations were then carried out, including cutting tofu with a knife (Fig. 5(e)) and unlocking a locker with a key (Fig. 5(f)). In the cutting experiment, the robot gripped a knife and cut tofu three times (Movie S4). The friction between the knife and the fingers was monitored to determine whether the knife was cutting the tofu or touching the cutting board. When the blade touched the tofu, the upward resistance induced a slight increase of F_y. Since the tofu was soft and homogenous, the force in all three directions remained stable during the cutting process (see the blue columns in Fig. 5(e)). As the knife continued to move downward, it was eventually blocked by the cutting board. Instantaneously, F_y soared above a safety threshold, triggering the robot to
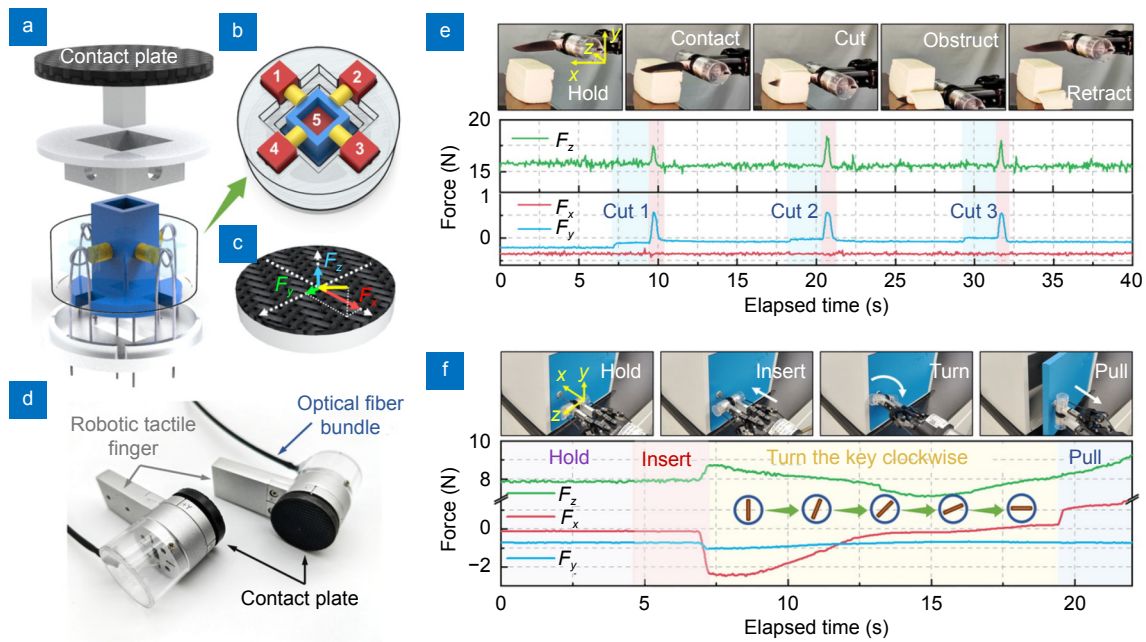
Fig. 5 | Dexterous manipulation based on tri-axial force sensing. (**a**) Exploded diagram of the robotic tactile finger. (**b**) Positions of the five OFN sensors inside the finger. (**c**) Schematic diagram of force decomposition. (**d**) Photograph of two robotic tactile fingers. (**e**, **f**) The tri-axial force sensing signals and snapshots during the cutting experiment and the unlocking experiment, respectively.

retract the knife (see the red columns in Fig. 5(e)). We also noticed jumps in the signal of F_z, which were probably due to the tilt of the knife when the blade contacted the cutting board.

Next, we commanded the robot to unlock a locker with a key (Fig. 5(f) and Movie S5). To determine whether the key was fully inserted, we monitored the horizontal frictional force (F_x) between the key and the fingers. The force signals demonstrated that once the key was completely inserted into the keyhole, F_x changed rapidly from nearly zero to below –2 N. Thereafter, the robot turned the key 90° and pulled it to open the locker, resulting in an increase in F_x in the opposite direction. Another friction component F_y and the grip force F_z varied accordingly during the unlocking process. Since F_x was more straightforward to understand in this experiment, we regarded it as the key variable in the robotic control program.

Conclusions

In this article, we reported a straightforward and cost-effective strategy for developing tactile sensors based on OFNs. The tangled structure of the knot alters the load distribution along the fiber, enabling the OFN sensor to detect slip and measure friction in dexterous robotic manipulation. To detect slip during adaptive grasping, we fixed flat OFN sensors onto a robotic finger, and pro-

cessed the vibrating signal with a customized slip detection algorithm. To measure tri-axial forces in dexterous manipulation, we devised a highly integrated robotic finger enclosing multiple cubic OFN sensors, with each sensor detecting forces from various directions. For clarity, we itemize the contributions of this work as follows: 1) We introduced the knotted structure and investigated its sensing capabilities to both normal and frictional forces. 2) We demonstrated an application of the fiber knot sensor and validated its potential for tactile sensing in robotics.

Although OFN sensors prove to be valuable for slip and friction measurement, this approach has several limitations. One of the main challenges is that OFN is unable to withstand high temperatures owing to the limited thermal stability of long-chain polymers. PMMA, for example, has a glass transition temperature of 100 °C and begins to soften at about 90 °C. Working at high temperatures results in irreversible damage to the sensor. However, by employing optical fibers made of materials like PC (polycarbonate) with higher softening temperatures, the sensor can function within an extended range of temperature.

Lastly, it is possible to weave a compliant tactile web composed of multiple optical fibers to cover complex curved surfaces, such as the fingertips, palms, arm joints, and feet of a robot. This flexible web can provide distrib-

uted pressure and friction information over the robot, which might be helpful for dexterous manipulation, human-machine interaction, and biped locomotion in the future.

References

1. Mason MT. Toward robotic manipulation. *Ann Rev Control Robot Auton Syst* **1**, 1–28 (2018).

2. Billard A, Kragic D. Trends and challenges in robot manipulation. *Science* **364**, eaat8414 (2019).

3. Cui JD, Trinkle J. Toward next-generation learned robot manipulation. *Sci Robot* **6**, eadb9461 (2021).

4. Sundaram S. How to improve robotic touch. *Science* **370**, 768–769 (2020).

5. Zhong F, Hu W, Zhu PN, Wang H, Ma C et al. Piezoresistive design for electronic skin: from fundamental to emerging applications. *Opto-Electron Adv* **5** (2022).

6. Liu FY, Deswal S, Christou A, Sandamirskaya Y, Kaboli M et al. Neuro-inspired electronic skin for robots. *Sci Robot* **7**, eabl7344 (2022).

7. Li GZ, Liu SQ, Wang LQ, Zhu R. Skin-inspired quadruple tactile sensors integrated on a robot hand enable object recognition. *Sci Robot* **5**, eabc8134 (2020).

8. Liu FY, Deswal S, Christou A, Shojaei Baghini M, Chirila R et al. Printed synaptic transistor-based electronic skin for robots to feel and learn. *Sci Robot* **7**, eabl7286 (2022).

9. Zhao ZX, Tang JS, Yuan J, Li YJ, Dai Y et al. Large-scale integrated flexible tactile sensor array for sensitive smart robotic touch. *ACS Nano* **16**, 16784–16795 (2022).

10. Liu YF, Cui SW, Wei JH, Li HB, Hu JY et al. Centrosymmetric- and axisymmetric-patterned flexible tactile sensor for roughness and slip intelligent recognition. *Adv Intellig Syst* **4**, 2100072 (2021).

11. Wang YC, Wu X, Mei DQ, Zhu LF, Chen JN. Flexible tactile sensor array for distributed tactile sensing and slip detection in robotic hand grasping. *Sens Actuat A Phys* **297**, 111512 (2019).

12. Cao YD, Li T, Gu Y, Luo H, Wang SQ et al. Fingerprint-inspired flexible tactile sensor for accurately discerning surface texture. *Small* **14**, 1703902 (2018).

13. Yan YC, Hu Z, Yang ZB, Yuan WZ, Song CY et al. Soft magnetic skin for super-resolution tactile sensing with force self-decoupling. *Sci Robot* **6**, eabc8801 (2021).

14. Dwivedi A, Ramakrishnan A, Reddy A, Patel K, Ozel S et al. Design, modeling, and validation of a soft magnetic 3-D force sensor. *IEEE Sens J* **18**, 3852–3863 (2018).

15. Xie SP, Zhang YF, Zhang H, Jin MH. Development of triaxis electromagnetic tactile sensor with adjustable sensitivity and measurement range for robot manipulation. *IEEE Trans Instrum Meas* **71**, 1–9 (2022).

16. Barreiros JA, Xu A, Pugach S, Iyengar N, Troxell G et al. Haptic perception using optoelectronic robotic flesh for embodied artificially intelligent agents. *Sci Robot* **7**, eabi6745 (2022).

17. Ward-Cherrier B, Pestell N, Cramphorn L, Winstone B, Giannaccini ME et al. The TacTip family: soft optical tactile sensors with 3D-printed biomimetic morphologies. *Soft Robot* **5**, 216–227 (2018).

18. Yuan WZ, Dong SY, Adelson EH. GelSight: high-resolution robot tactile sensors for estimating geometry and force. *Sensors* **17**, 2762 (2017).

19. Biazi-Neto V, Marques CAF, Frizera-Neto A, Leal-Junior AG. FBG-embedded robotic manipulator tool for structural integrity monitoring from critical strain-stress pair estimation. *IEEE Sens J* **22**, 5695–5702 (2022).

20. Biazi-Neto V, Marques CAF, Frizera-Neto A, Leal-Junior AG. FBG-based sensing system to improve tactile sensitivity of robotic manipulators working in unstructured environments. *Sens Actuat A Phys* **359**, 114473 (2023).

21. Borràs J. Effective grasping enables successful robot-assisted dressing. *Sci Robot* **7**, eabo7229 (2022).

22. Shih B, Shah D, Li JX, Thuruthel TG, Park YL et al. Electronic skins and machine learning for intelligent soft robots. *Sci Robot* **5**, eaaz9239 (2020).

23. Koo JH, Yun HW, Lee WC, Sunwoo SH, Shim HJ et al. Recent advances in soft electronic materials for intrinsically stretchable optoelectronic systems. *Opto-Electron Adv* **5**, 210131 (2022).

24. Ding ZM, Zhang ZY. 2D tactile sensor based on multimode interference and deep learning. *Opt Laser Technol* **136**, 106760 (2021).

25. Pan J, Zhang Z, Jiang CP, Zhang L, Tong LM. A multifunctional skin-like wearable optical sensor based on an optical micro-/nanofibre. *Nanoscale* **12**, 17538–17544 (2020).

26. Van Meerbeek IM, De Sa CM, Shepherd RF. Soft optoelectronic sensory foams with proprioception. *Sci Robot* **3**, eaau2489 (2018).

27. Leal-Junior A, Avellar L, Biazi V, Soares MS, Frizera A et al. Multifunctional flexible optical waveguide sensor: on the bioinspiration for ultrasensitive sensors development. *Opto-Electron Adv* **5**, 210098 (2022).

28. Yu W, Yao N, Pan J, Fang W, Li X et al. Highly sensitive and fast response strain sensor based on evanescently coupled micro/nanofibers. *Opto-Electron Adv* **5**, 210101 (2022).

29. Li LY, Liu YF, Song CY, Sheng SF, Yang LY et al. Wearable alignment-free microfiber-based sensor chip for precise vital signs monitoring and cardiovascular assessment. *Adv Fiber Mater* **4**, 475–486 (2022).

30. Zhao HC, O'Brien K, Li S, Shepherd RF. Optoelectronically innervated soft prosthetic hand via stretchable optical waveguides. *Sci Robot* **1**, eaai7529 (2016).

31. Teeple CB, Becker KP, Wood RJ. Soft curvature and contact force sensors for deep-sea grasping via soft optical waveguides. In *2018 IEEE/RSJ International Conference on Intelligent Robots and Systems* 1621–1627 (IEEE, 2018); http://doi.org/10.1109/IROS.2018.8594270.

32. Zhang L, Pan J, Zhang Z, Wu H, Yao N et al. Ultrasensitive skin-like wearable optical sensors based on glass micro/nanofibers. *Opto-Electron Adv* **3**, 190022 (2020).

33. Tang Y, Yu LT, Pan J, Yao N, Geng WD et al. Optical nanofiber skins for multifunctional humanoid tactility. *Adv Intellig Syst* **5**, 2200203 (2023).

34. Yao N, Wang XY, Ma SQ, Song XD, Wang S et al. Single optical microfiber enabled tactile sensor for simultaneous temperature and pressure measurement. *Photon Res* **10**, 2040–2046 (2022).

35. Massari L, Fransvea G, D'Abbraccio J, Filosa M, Terruso G et al. Functional mimicry of Ruffini receptors with fibre Bragg gratings and deep neural networks enables a bio-inspired large-area tactile-sensitive skin. *Nat Mach Intellig* **4**, 425–435 (2022).

36. Bai HD, Li S, Barreiros J, Tu YQ, Pollock CR et al. Stretchable

distributed fiber-optic sensors. *Science* **370**, 848–852 (2020).

37. Lee B. Review of the present status of optical fiber sensors. *Opt Fiber Technol* **9**, 57–79 (2003).

38. Li YP, Tan SJ, Yang LY, Li LY, Fang F et al. Optical microfiber neuron for finger motion perception. *Adv Fiber Mater* **4**, 226–234 (2022).

39. Jiang CP, Zhang Z, Pan J, Wang YC, Zhang L et al. Finger-skin-inspired flexible optical sensor for force sensing and slip detection in robotic grasping. *Adv Mater Technol* **6**, 2100285 (2021).

40. Zhou JY, Shao Q, Tang C, Qiao F, Lu TQ et al. Conformable and compact multiaxis tactile sensor for human and robotic grasping via anisotropic waveguides. *Adv Mater Technol* **7**, 2200595 (2022).

41. Patil VP, Sandt JD, Kolle M, Dunkel J. Topological mechanics of knots and tangles. *Science* **367**, 71–75 (2020).

42. Takeuchi J, Yamanishi K. A unifying framework for detecting outliers and change points from time series. *IEEE Trans Knowledge Data Eng* **18**, 482–492 (2006).

43. Nan KW, Babaee S, Chan WW, Kuosmanen JLP, Feig VR et al. Low-cost gastrointestinal manometry via silicone-liquid-metal pressure transducers resembling a quipu. *Nat Biomed Eng* **6**, 1092–1104 (2022).

44. Zhang HP, Oh S, Mahato M, Yoo H, Oh IK. Knot‐architectured fabric actuators based on shape memory fibers. *Adv Funct Mater* **32**, 2205732 (2022).

45. Xie Y, Cai DW, Wu H, Pan J, Zhou N et al. Mid-infrared chalcogenide microfiber knot resonators. *Photon Res* **8**, 616–621

46. Wang WJ, Yiu HHP, Li WJ, Roy VAL. The principle and architectures of optical stress sensors and the progress on the development of microbend optical sensors. *Adv Opt Mater* **9**, 2001693 (2021).

Acknowledgements

Author contributions

J. Pan, L. Zhang and L. T. Yu conceived the project idea and designed the experiments. J. Pan, Q. Wang, S. K. Gao, and Z. Zhang carried out the experiments and collected the data. J. Pan and Y. Xie contributed to the finite-element simulations. All authors discussed the results and commented on the manuscript.

Competing interests

The authors declare no competing financial interests.

Supplementary information

Supplementary information for this paper is available at
https://doi.org/10.29026/oea.2023.230076